crystals

MDPI

Article

Low-Cost Foamed Ceramics with Enhanced Mechanical Performance and Uniform Pore Size Structure

Junchi Weng [1], Xiulin Shen [1,2,3,4,*], Yixian Yang [1], Xuejia Zhang [1], Mengke Fan [1], Ge Gao [1], Zeming Guo [1], Zhenfei Lv [1,2,3,4,*] and Xiujuan Feng [2,*]

[1] School of Materials Science and Engineering, Anhui University of Science and Technology, Huainan 232001, China; 2024201050@aust.edu.cn (J.W.); yyx@aust.edu.cn (Y.Y.); xuejiazhang@aust.edu.cn (X.Z.); fmk@aust.edu.cn (M.F.); gao_ge_123@163.com (G.G.); 2023303837@aust.edu.cn (Z.G.)
[2] Key Laboratory of Industrial Dust Prevention and Control & Occupational Health and Safety, Ministry of Education, Anhui University of Science and Technology, Huainan 232001, China
[3] Anhui Industrial Generic Technology Research Center for New Materials from Coal-Based Solid Wastes, Huainan 232001, China
[4] Anhui International Joint Research Center for Nano Carbon-Based Materials and Environmental Health, Huainan 232001, China
* Correspondence: xlshen@aust.edu.cn (X.S.); zflv@aust.edu.cn (Z.L.); fengxj.2011@tsinghua.org.cn (X.F.)

Abstract: Due to the lack of effective utilization, fly ash and red mud accumulate in large quantities and cause serious harm to the environment. In this experiment, a low-cost preparation of foamed ceramics was realized by applying the foaming agent addition method using fly ash and red mud. The results indicated that temperature and foaming agent content significantly affected the macrostructure, microstructure, crystalline phases, and properties of the foamed ceramics. Specifically, a formulation comprising 45 wt.% fly ash, 45 wt.% red mud, 10 wt.% clay, and 1 wt.% SiC (addition), sintered at 1210 °C, yielded a compressive strength of 8.2 MPa, a bulk density of 1.17 g/cm^3, a water absorption rate of 32.05%, and an apparent porosity of 37.59%. The as-prepared materials demonstrate potential as cost-effective building materials, putting forward an effective approach for the high-value utilization of fly ash and red mud.

Keywords: foamed ceramics; fly ash; red mud; silicon carbide; sintering temperature

check for updates

Academic Editor: Francisco M. Morales

Received: 17 January 2025
Revised: 8 February 2025
Accepted: 10 February 2025
Published: 13 February 2025

Citation: Weng, J.; Shen, X.; Yang, Y.; Zhang, X.; Fan, M.; Gao, G.; Guo, Z.; Lv, Z.; Feng, X. Low-Cost Foamed Ceramics with Enhanced Mechanical Performance and Uniform Pore Size Structure. *Crystals* **2025**, *15*, 180. https://doi.org/10.3390/cryst15020180

Copyright: © 2025 by the authors. Licensee MDPI, Basel, Switzerland. This article is an open access article distributed under the terms and conditions of the Creative Commons Attribution (CC BY) license (https://creativecommons.org/licenses/by/4.0/).

1. Introduction

Coal is an important component of the global energy structure [1], supplying a significant proportion for the economy, society, and construction [2–4]. Nevertheless, the massive consumption of coal resources is inevitably accompanied by the generation of vast amounts of coal-based solid waste, such as coal gangue, fly ash, and coal gasification slag. Fly ash, a by-product of coal combustion in power plants [5], is classified as a hazardous substance worldwide. Billions of tones of fly ash have been generated annually from thermal power plants, resulting in serious issues regarding land disposal and environmental contamination [6]. Therefore, it is imperative to explore new applications for fly ash to mitigate environmental pollution and facilitate high-value-added products [7].

Red mud is a significant solid waste generated during the extraction of alumina from bauxite ore [8,9]. For every ton of alumina produced, approximately 1 to 1.5 tons of red mud is generated [10]. It poses serious environmental challenges due to its corrosive nature [4]. At present, a few experiments have investigated the laboratory application of red mud as a cementitious material, but it still lacks basis for large-scale practical application limited by the relatively high content of heavy metals and uneven chemical composition [11]. The

remainder is discharged directly into ponds or landfills, which is detrimental to sustainable development, leading to an unproductive use of land resources. This practice also imposes ongoing economic pressure for long-term maintenance.

A multitude of studies have delved into the reuse of red mud and fly ash. For instance, Li et al. [12] reported experimental findings on the use of red mud and fly ash for the removal of toxic substances from waste. Karasu et al. [13] examined the effect of red mud-based pigments on the glaze of ceramic and floor tiles. However, the utilization of fly ash and red mud in the above research is relatively low, which is seriously inconsistent with their production. To promote the bulk utilization of red mud and fly ash, recent research has concentrated on building industries [14], particularly in the development of lightweight building products, such as foamed ceramics. Since their first production by Saint-Gobain in 1935 [15–20], foamed ceramics have been widely used in sound absorption, wave absorption, thermal insulation, and photoelectric sensors [21–23]. The porous three-dimensional networks contributed to the exceptional properties of foamed ceramics, including heat insulation, sound insulation, and high-temperature resistance [24–28]. Consequently, the development of foamed ceramics, utilizing fly ash and red mud as substitutes for tailings and quartz, has emerged as a significant focus within the domains of low-cost materials and resource reuse [29–33].

H. Cengizler et al. [34] prepared low thermal conductivity ceramic glass foams by sintering using fly ash with sodium silicate as a foaming agent and flux. The material exhibits a porosity ranging from 69.76% to 75.43%, a bulk density between 0.55 and 0.69 g/cm^3, a compressive strength from 3.2 to 5.35 MPa, and a thermal conductivity of 0.10 to 0.21 W/(m·K). Luo et al. [35] proposed a new method to convert fly ash into foamed ceramics, which was made possible by alkaline-activated pretreatment of the fly ash was self-foamed during the sintering process, and the prepared foamed ceramics showed the best performance when sintered at 1200 °C, with an apparent density of 0.41 g/cm^3, a porosity of 83.60%, a compressive strength of 8.3 MPa, and a thermal conductivity of 0.0983 W/(m·K). Xia et al. [36] prepared foamed ceramics by the direct foaming method at 1080–1120 °C using red mud and potassium feldspar washing waste as raw materials, and silicon carbide as foaming agent, when the KFW/RM ratio was 1:1, with a SiC content of 1 wt.%, sintering temperature of 1100 °C, and sintering time of 60 min; the bulk density of the foamed ceramics was 0.77 g/cm^3, the apparent porosity was 61.89%, the average pore size was 0.52 mm, and the compressive strength was 3.64 MPa. It can be found that solid waste has great potential in foamed ceramics products.

Nevertheless, foamed ceramics still suffer from compositional inhomogeneity and property instability due to complex and fluctuating components. Moreover, single utilization of solid waste strongly limits their large-scale production and performance enhancement [37]. In this study, foamed ceramics were prepared using fly ash and red mud as the main materials, and the effects of foaming agent content and temperature on the linear expansion rate, vertical expansion rate, apparent porosity, bulk density, water absorption, and compressive strength of foamed ceramics were investigated. The results indicated that the foamed ceramic produced with 1 wt.% SiC exhibited the most homogeneous pore distribution and optimal properties at a sintering temperature of 1210 °C. Specifically, its compressive strength, bulk density, apparent porosity, water absorption, linear expansion rate, and vertical expansion rate were measured at 8.2 MPa, 1.173 g/cm^3, 37.58%, 32.06%, 18.93%, and 151.83%, respectively. This can significantly reduce the cost of foamed ceramics and effectively improve their properties such as compressive strength and water absorption.

2. Materials and Methods

2.1. Raw Materials

Class I fly ash (produced from coal, classified as Sialic and Inert type according to Vassilev's chemical and phase classification, respectively) sourced from a power plant in Jinan, red mud obtained from the Ling Shou Yixin Mineral Products Processing Plant, and clay from the Yangquan Huayicheng Refractories Factory were utilized as raw materials. Polyvinyl alcohol (PVA, Aladdin, China) served as the binder, while silicon carbide (Tianjin Yetai, Sanhui, China) acted as the foaming agent.

2.2. Experimental Procedure

As depicted in Figure 1, the main experimental steps were as follows: Firstly, the raw materials were weighed according to the experimental formula (as shown in Table 1). Secondly, fly ash, red mud, and clay were homogeneously mixed, after which polyvinyl alcohol (PVA) and varying amounts of SiC were added and mixed again. Next, the mixed powder was compressed into cylindrical samples with a diameter and height of 15 mm using a powder compactor set at 10 MPa for 90 s. The samples were dried at 100 °C for 6 h using a blast drying oven (Huadeli, DGT-G80, Hefei, China), and subsequently sintered in a box resistance furnace (Kejing, KSL1700, Hefei, China). The sintering regime was as follows: the temperature was increased from room temperature to 1000 °C at a heating rate of 10 °C/min, followed by increments to 1200 °C (series A), 1210 °C (series B), and 1220 °C (series C) at a heating rate of 5 °C/min, respectively, with a holding time of 3 h before cooling naturally in the furnace.

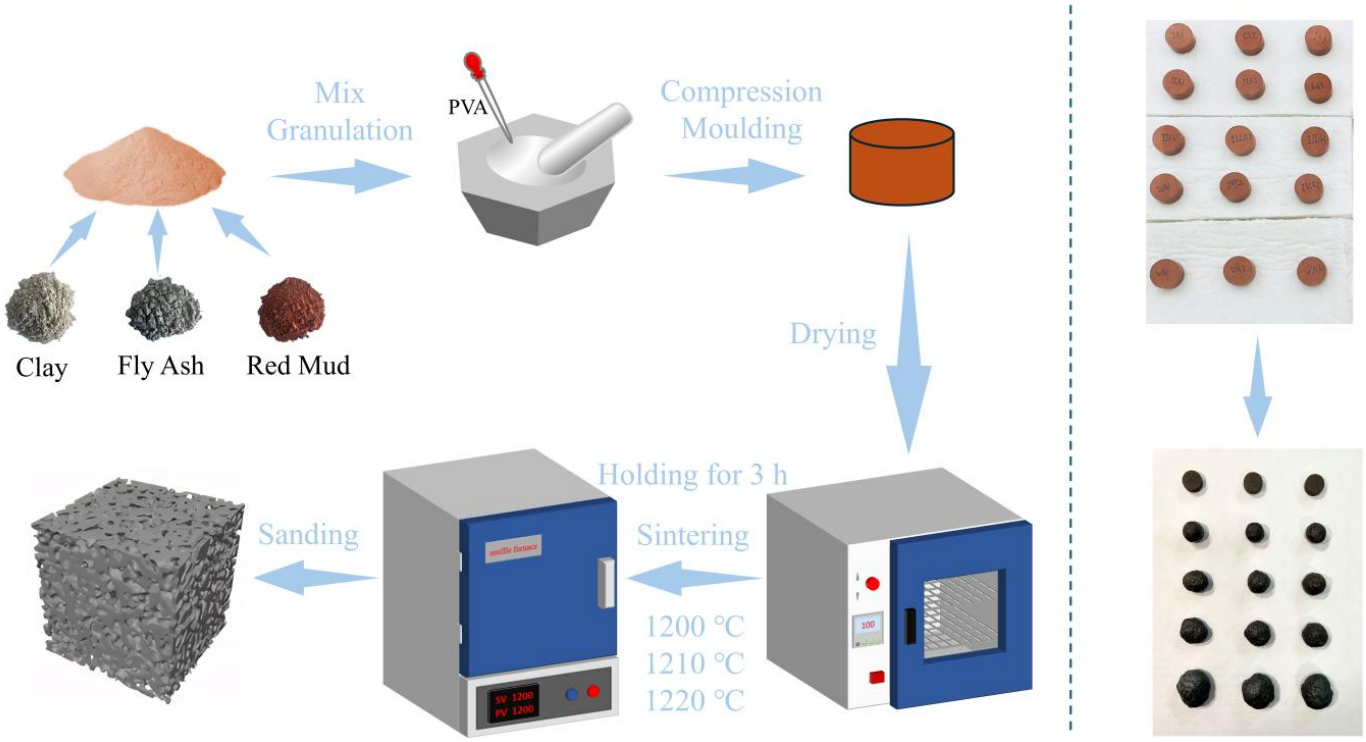

Figure 1. The preparation schematic diagram of foamed ceramics.

Table 1. Specimen formulations.

Number, X = A (1200 °C), B (1210 °C), C (1220 °C)	Fly Ash /wt.%	Red Mud/wt.%	Clay/wt.%	SiC (Addition)/wt.%	Binder Agent (Addition)/wt.%
X1	45	45	10	0	10
X2	45	45	10	0.5	10
X3	45	45	10	1.0	10
X4	45	45	10	1.5	10
X5	45	45	10	2.0	10

2.3. Characterization

2.3.1. Water Absorption, Bulk Density, and Apparent Porosity

The water absorption, bulk density, and apparent porosity of the foamed ceramics were determined using the boiling method. Initially, the foamed ceramics were dried in an oven at 60 °C until a constant weight was achieved, with this mass designated as m_1. The sample was then boiled in distilled water for 2 h, after which the mass of the sample submerged in water was measured using a density balance, recorded as m_2. Following this, the sample surface was wiped up, resulting in a mass of m_3. Consequently, the water absorption (W), bulk density (D), and porosity (P) of the foamed ceramics can be calculated using Equations (1), (2), and (3), respectively [30].

$$W = \frac{m_3 - m_1}{m_1} \times 100\% \quad (1)$$

$$D = \frac{m_1}{m_3 - m_2} \times \rho_1 \quad (2)$$

$$P = \frac{m_3 - m_1}{m_3 - m_2} \times 100\% \quad (3)$$

where m_1 is the mass of dried foamed ceramics, g; m_2 is the mass in water, g; m_3 is the mass saturated water, g.

2.3.2. Linear and Vertical Expansion Rates

The linear expansion rate represents the ratio of the change in length of ceramic body in one direction due to temperature change to its original length, and the vertical expansion rate is the ratio of the change in length of ceramic body in the vertical direction due to temperature change to its original length. The linear and vertical expansion rates of the samples were assessed using Equations (4) and (5), respectively. To ensure the reliability and accuracy of the data, each property was analyzed in triplicate [36].

$$L_e = \left(1 - \frac{L_f}{L_g}\right) \times 100\% \quad (4)$$

$$V_e = \left(1 - \frac{V_f}{V_g}\right) \times 100\% \quad (5)$$

L_e (%), L_f (mm), and L_g (mm) represent the linear expansion rate of the foamed ceramics, the diameter of the green body (15 mm), and the diameter of the sintered sample, respectively.

V_e (%), V_f (mm), and V_g (mm) indicate the vertical expansion rate of the foamed ceramics, the thickness of the green body (~6 mm), and the thickness of the sintered sample, respectively.

2.3.3. Analysis of Raw Material Composition

An X-ray fluorescence spectrometer (XRF, Tianrui, EDX4500H, Kunshan, China) was employed to determine the substance composition and elemental ratios. The following are the parameters of the XRF test: tube voltage (40 kV), tube current (100 mA), initialisation element (Ag).

2.3.4. Phase Analysis

Phase analysis of the material was conducted using an X-ray diffractometer (XRD, Rigaku Smart lab, Akishima-shi, Japan). The following are the parameters of the XRD test: tube voltage 40 kV, tube current 200 μA, Cu target, diffraction width DS = SS = 1°, RS = 0.3 mm, scanning speed $7^\circ \cdot min^{-1}$, scanning range 3~80°.

2.3.5. Microstructure Characterization

The microstructure of the samples was examined using an SU8600 scanning electron microscope (SEM, Rili, SU8600, Shanghai, China). The acceleration voltage was set to 3 kV for morphology imaging and 15 kV for energy spectrum mapping, with the SE2 secondary electron detector being used.

2.3.6. Compressive Strength

The compressive strength of the samples was evaluated using a universal testing machine (Puye, WDW-3T, Jinan, China), which measured 9 × 9 × 9 mm. The compressive strength of the specimen is calculated according to Equation (6) [38].

$$R_C = \frac{P}{S} \tag{6}$$

where R_C is the compressive strength, MPa; P is the specimen breaking load, N; S is the specimen force area, mm^2.

3. Results and Discussion

3.1. Chemical and Phase Composition of Raw Materials

The chemical compositions of fly ash and red mud are presented in Table 2. Fly ash predominantly consists of SiO_2 (54.09 wt.%) and Al_2O_3 (30.80 wt.%), with relatively low concentrations of other chemical components, which is a characteristic feature of fly ash [39]. Red mud exhibits a high content of Fe_2O_3 (36.19 wt.%) and Al_2O_3 (19.44 wt.%). In terms of crystalline phases (Figure 2), sillimanite (Al_2SiO_5, PDF#00-038-0471), quartz (SiO_2, PDF#00-003-1161), and mullite ($3Al_2O_3 \cdot 2SiO_2$, PDF#00-015-0776) are identified as the main crystalline phases in fly ash. Mullite ($3Al_2O_3 \cdot 2SiO_2$, PDF#00-015-0776), cristobalite (SiO_2, PDF#00-082-0512), and kaolinite ($2SiO_2 \cdot Al_2O_3 \cdot 2H_2O$, PDF#00-014-0164) are the main crystalline phases in clay. Meanwhile, hematite (Fe_2O_3, PDF#00-001-1053) is present in the red mud, as well as calcite ($CaCO_3$, PDF#00-072-1651) and pyrophyllite ($Al_2[Si_4O_{10}](OH)_2$, PDF#00-074-1193).

Table 2. Chemical compositions of fly ash, clay, and red mud (wt.%).

Component	Mass Fraction/wt.%								
	Na_2O	MgO	Al_2O_3	SiO_2	Fe_2O_3	SO_3	K_2O	CaO	TiO_2
Fly ash	0.59	0.85	30.80	54.09	4.68	0.86	2.28	3.93	1.32
Clay	0.62	0.94	50.36	36.59	4.62	0.05	0.41	0.73	2.39
Red mud	5.57	5.69	19.44	18.75	36.19	0.68	0.50	7.82	4.42

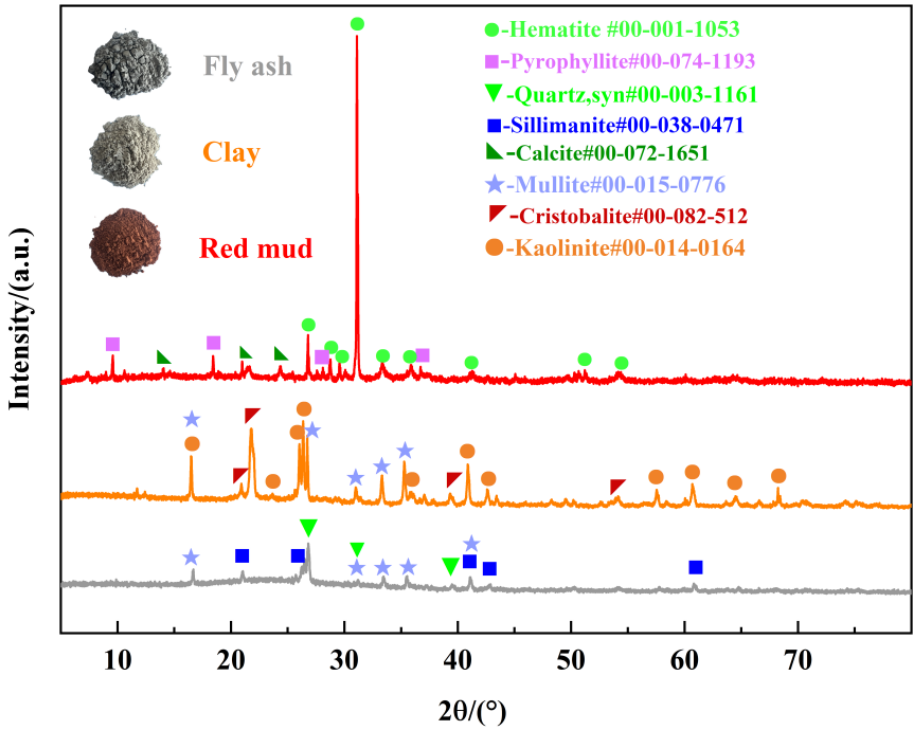

Figure 2. XRD patterns of fly ash, clay, and red mud.

3.2. Macrostructure and Expansion Rates of Foamed Ceramics

Figure 3a–e illustrates the macrostructures and expansion rates of the samples prepared at various sintering temperatures and SiC content ratios. It is obvious that these factors have a significant effect on the macrostructure and expansion rates of the samples. With the rise of SiC content (see Figure 3a–c), the linear expansion rates of the samples showed a gradual increase (from 0–40%, 0–45%, and 0–55%, respectively), while the vertical expansion rate showed an increase and then a decrease (from 0–100–90%, 0–150–82%, and 0–130–90%, respectively). Obviously, the sample added with 1 wt.% SiC exhibits the most effective foaming characteristics (linear, vertical expansion rate at three temperatures of 7%, 100%; 19%, 150%; and 27%, 130%, respectively). While a high linear expansion rate does not necessarily correlate with superior expansion, it is observed that the internal small pores coalesce into larger ones, leading to the bulging of the sample. This phenomenon is particularly evident in the sample sintered at 1210 °C (with 1 wt.% SiC), which demonstrates a higher vertical expansion rate, resulting in a more pronounced three-dimensional foaming effect. With increasing temperature (see Figure 3d,e), the linear expansion (from 1.2–13%, 2–33%, respectively) of the samples (containing 0.5 wt.%, 1 wt.% SiC) gradually increases, while the vertical expansion rate (from 65–135–125%, 137–155–125%, respectively) increases and then decreases. It can be hypothesized that when the temperature is lower, the samples do not foam sufficiently, whereas when the temperature is higher, the reactions occurring inside the samples are more active, and the resulting CO_2 gas overflow leads to the collapse of the samples. Specially, samples sintered at 1220 °C with 2 wt.% SiC demonstrate larger pores and a higher vertical expansion rate owing to the high temperature and the high SiC content. These factors influence the viscosity and content of the glass phase, as well as the amount of CO_2 generated. Consequently, they lead to changes in the internal pore structure of the ceramics, resulting in an increased expansion rate.

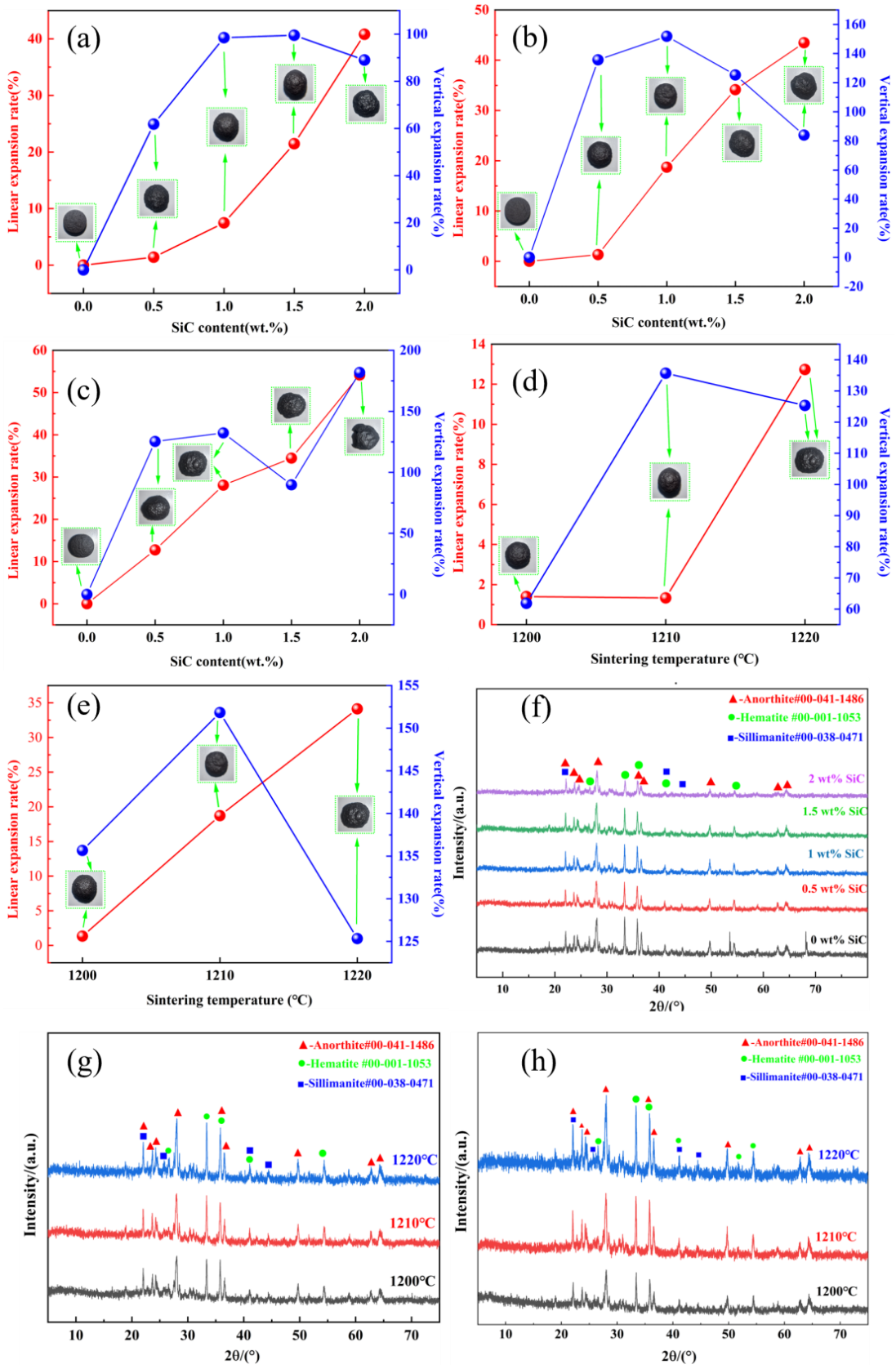

Figure 3. Macrostructure, linear expansion rates, and vertical expansion rates of samples sintered at (**a**) 1200 °C, (**b**) 1210 °C, and (**c**) 1220 °C, alongside differing SiC contents: (**d**) 0.5 wt.% SiC and (**e**) 1 wt.% SiC; XRD patterns of samples sintered at (**f**) 1210 °C with different SiC contents, sintered at different temperatures with: (**g**) 0.5 wt.% SiC, (**h**) 1 wt.% SiC.

3.3. Crystalline Phase of Foamed Ceramics

The phase composition of foamed ceramics is fundamental in determining the occurrence of the sintering process [40]. Figure 3f–h presents the XRD patterns of the samples prepared at different sintering temperatures and SiC content ratios. XRD analysis reveals that all sintered samples include sillimanite (Al_2SiO_5, PDF#00-038-0471), hematite (Fe_2O_3, PDF#00-001-1053), and anorthite ($CaAl_2Si_2O_8$, PDF#00-041-1486). These three phases contribute to the material's favorable mechanical properties and exceptional high-temperature resistance. As the main phase in clay, kaolinite reacts to form metakaolin (550–850 °C) and then primary mullite (1050–1400 °C), respectively, during the high-temperature sintering process. The generation of sillimanite is produced by the reaction of alumina and silicon oxide in the raw material at temperatures between 700 °C and 900 °C. The formation of anorthite starts with calcium oxide, which derives from the glass phase in the raw materials and the decomposition of calcite at high temperatures. The following reactions gradually occur [38]:

$$CaO(s) + SiO_2(s) \rightarrow CaSiO_3(s) \quad (7)$$

$$2CaSiO_3(s) + Al_2O_3(s) + 3SiO_2(s) \rightarrow Ca_2Al_2(SiO_3)_5(s) \quad (8)$$

$$Ca_2Al_2(SiO_3)_5(s) + 8CaO(s) + 4Al_2O_3(s) \rightarrow 5Ca_2Al_2SiO_7(s) \quad (9)$$

$$Ca_2Al_2SiO_7(s) + Al_2O_3(s) + 3SiO_2(s) \rightarrow 2CaAl_2Si_2O_8(s) \quad (10)$$

The pyrophyllite in the raw material undergoes dehydration at 600–900 °C and decomposes into mullite and quartz at 1200 °C, which are not reflected in the picture because of their small content.

In Figure 3f, the diffraction peaks of the phases become sharper with the increase in temperature, indicating the increase in crystallinity. It is assumed that the increase in temperature will promote the chemical activity and migration rate of the reactants and activate the crystallization reaction. It can be found in Figure 3g,h that composition of the phases does not change much with the SiC content increase, indicating the ignorable effect of SiC on the phases.

3.4. Microstructure of Foamed Ceramics

Figure 4a illustrates the micromorphology of the pore structure in samples sintered at 1210 °C with varying SiC contents. (0%, 0.5 wt.%, 1 wt.%, 1.5 wt.%, and 2 wt.%). The results show that micropores appeared on the surface of samples. In addition, where visible, it is evident that no visible pore windows were formed on the inner surfaces of the pores, which suggests the domination of closed pores, reaching the most homogeneous at a SiC content of 1 wt.%. The small pores continuously merged to form connected open pores, which led to an increase in the diameter of the sample pores, which was favorable to the penetration of water molecules, and this coincided with the effect of SiC content on water absorption. The elemental distributions of B2 samples were determined by EDS (Figure 4b). The main elements identified were O, Si, Ca, Fe, and Al, which are consistent with the chemical composition analysis results of fly ash and red mud presented in Table 1. Moreover, an enrichment of Fe elements was observed, which is consistent with the existence of hematite analyzed by XRD, and can significantly enhance the brittleness of the samples and reduce the strength.

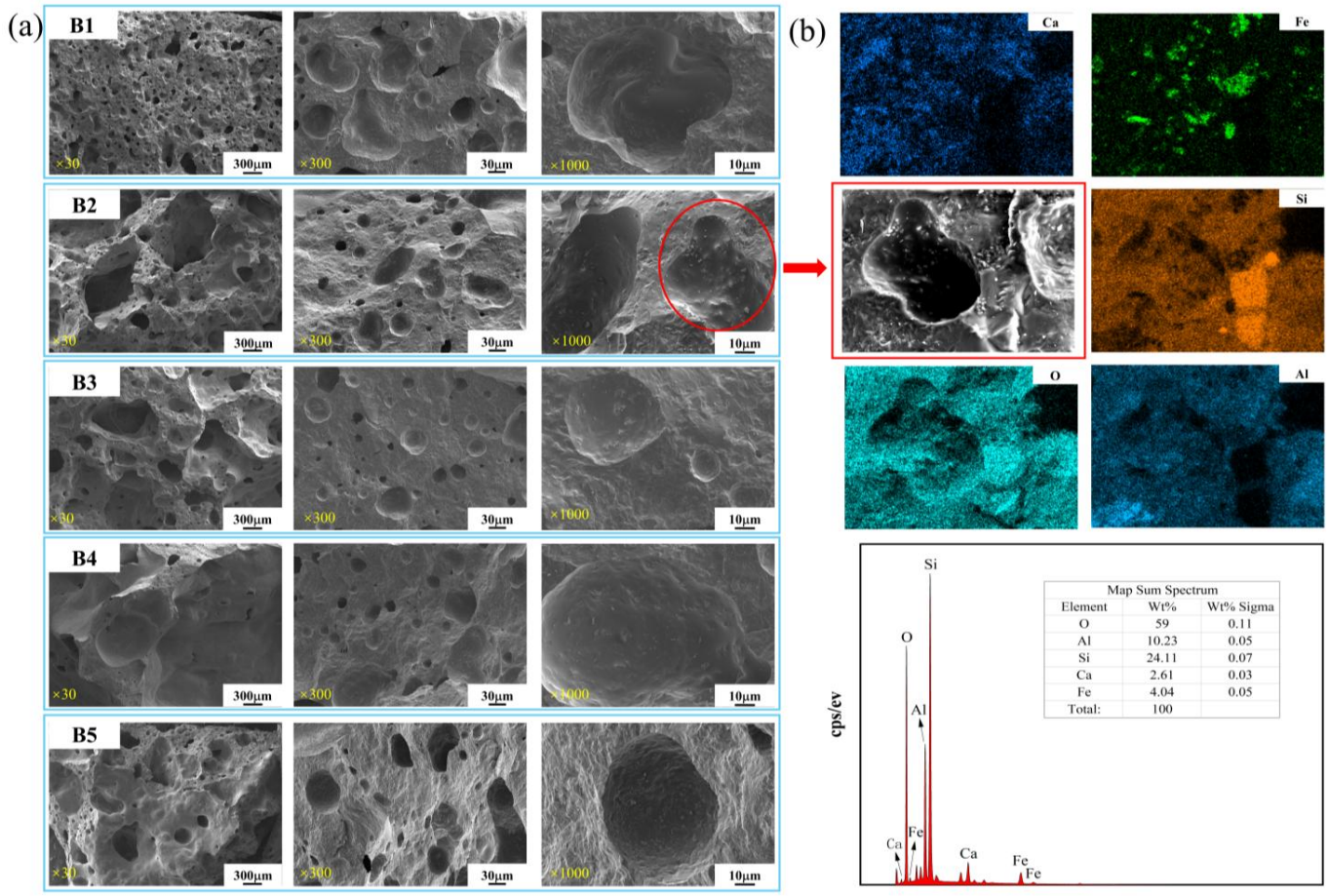

Figure 4. SEM and EDS images of samples with varying SiC contents at 1210 °C: (**a**) SiC contents of 0% (B1), 0.5 wt.% (B2), 1 wt.% (B3), 1.5 wt.% (B4), and 2 wt.% (B5), with resolution of ×30, ×300, and ×1000 from left to right, respectively; (**b**) the energy spectrum analysis of the sample with 0.5 wt.% SiC content.

Figure 5 illustrates the microscopic morphology of the pore structure of the samples added with 0.5 wt.% and 1 wt.% SiC at varying temperatures (1200 °C, 1210 °C, and 1220 °C). The results indicate firstly that as the temperature increases, the pore size gradually enlarges, accompanied by the formation of multiple smaller pores. Numerous small pores of varying sizes are present on the pore walls, predominantly as isolated structures. The overall foamed ceramics comprise pores, micropores, and pore walls. At elevated temperatures, the samples' surface begins to melt and soften. Concurrently, gas release initiates a foaming process, resulting in a significant increase in pore quantity within the sample. The particles within the sample bond together to form the pore walls. In addition, it can be seen that the pores of samples A3, B3, and C3 are more homogeneous compared to those of A2, B2, and C2, respectively, which can be attributed to the inconsistencies of SiC distribution and high-temperature melt viscosity.

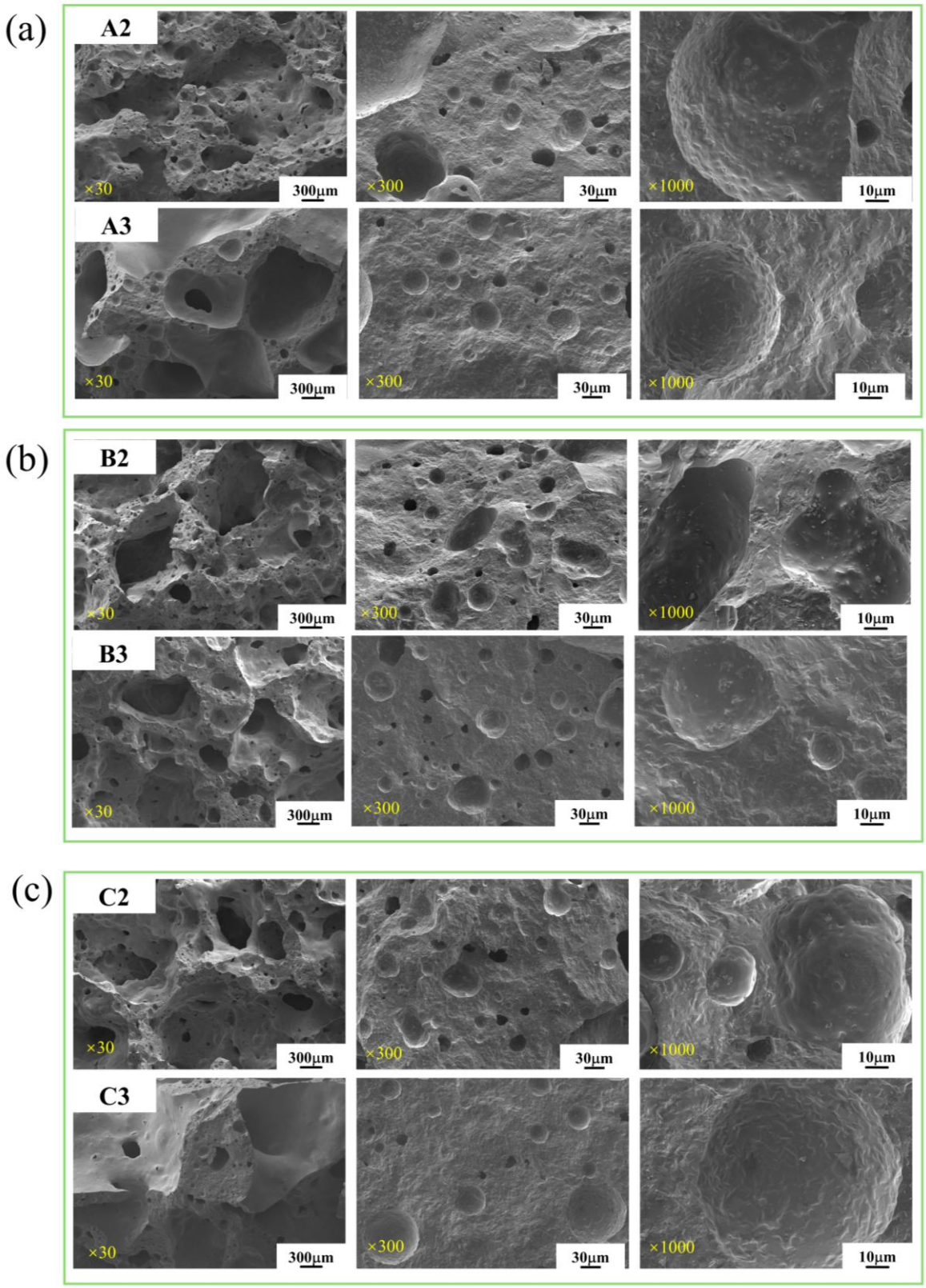

Figure 5. SEM images of samples added with SiC contents of 0.5 wt.% (A2, B2, C2), 1 wt.% (A3, B3, C3), with resolution of ×30, ×300, and ×1000 from left to right, respectively; taken at temperatures of: (**a**) 1200 °C, (**b**) 1210 °C, and (**c**) 1220 °C.

3.5. Physical Properties of Foamed Ceramics

Differences in the structure and crystalline phase of a material can significantly influence its properties. Therefore, we systematically evaluated the compressive strength, bulk density, apparent porosity, and water absorption of samples prepared with different SiC contents and sintering temperatures, as illustrated in Figure 6.

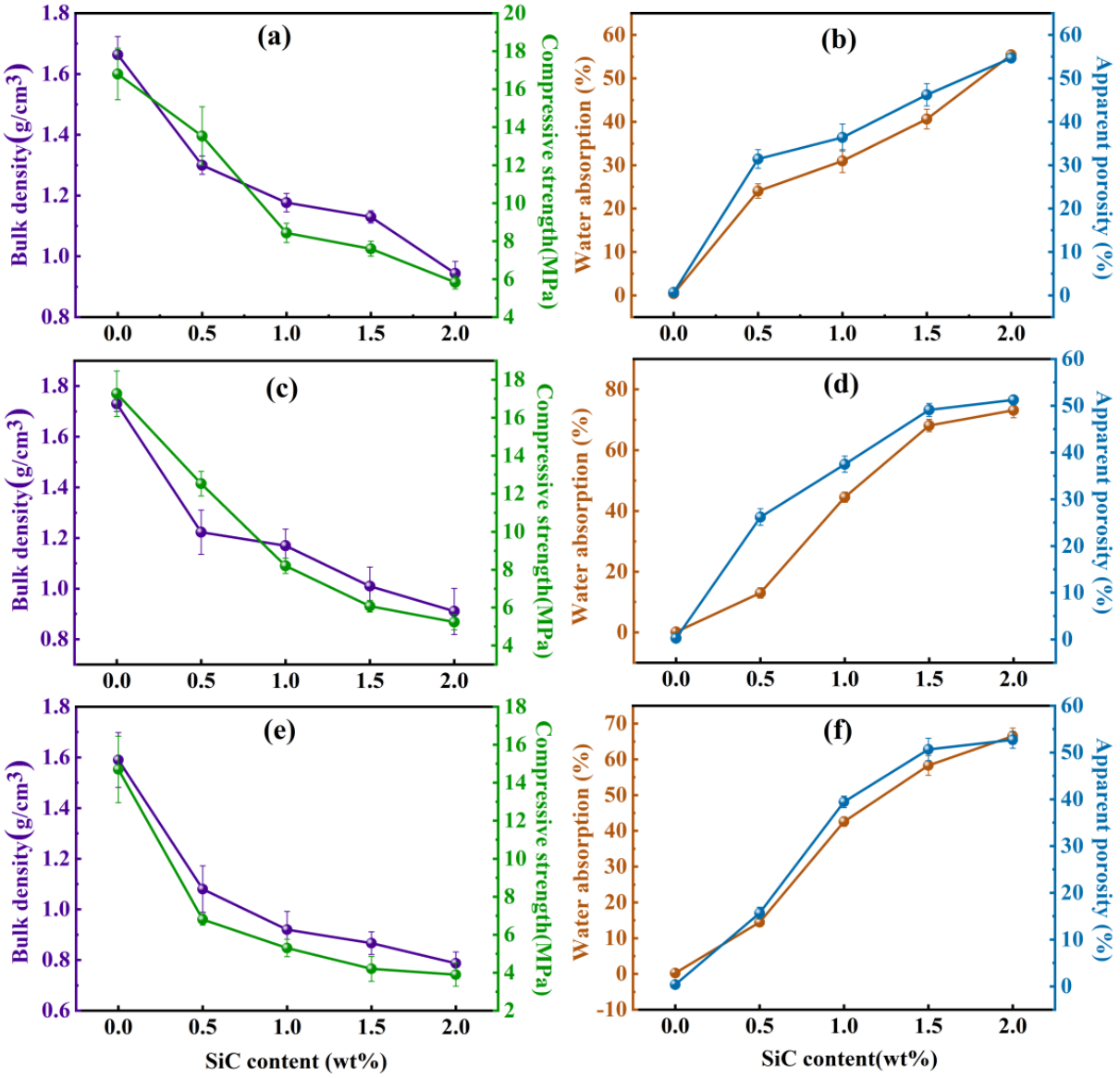

Figure 6. Compressive strength, bulk density, apparent porosity, and water absorption of foamed ceramics with different SiC contents (0%, 0.5 wt.%, 1 wt.%, 1.5 wt.%, 2 wt.%) sintered at: (**a**,**b**) 1200 °C, (**c**,**d**) 1210 °C, (**e**,**f**) 1220 °C.

The three sets of graphs illustrate the effects of different SiC content on the properties of the samples sintered at 1200 °C, 1210 °C, and 1220 °C, respectively. Notably, the bulk density and compressive strength of the sintered samples decreased with increasing SiC content at all temperatures. Specifically, the bulk density decreased from 1.68 g/cm^3 to 0.95 g/cm^3, from 1.73 g/cm^3 to 0.92 g/cm^3, and from 1.61 g/cm^3 to 0.79 g/cm^3 at the three temperatures. Similarly, the compressive strength decreased from 17.1 MPa to 5.9 MPa, from 16.9 MPa to 6.2 MPa, and from 15.4 MPa to 4.8 MPa. In contrast, water absorption and apparent porosity increased, with water absorption rising from 0% to 54%, from 0% to 71%, and from 0% to 66%, respectively, while apparent porosity increased from 0% to

56%, from 0% to 52%, and from 0% to 53%. By integrating the experimental results related to the crystalline phase and microstructure (Figures 3 and 4), it can be concluded that the change in compressive strength is primarily attributed to the change in porosity. In foamed ceramics, compressive strength typically decreases significantly with increasing porosity. This is because an increase in poverty implies a reduction in the continuous phase within the material, which in turn weakens the overall structural integrity and load-bearing capacity, thus weakening the overall load-bearing capacity of the material. In addition to porosity, the size of the pores also has a significant effect on the compressive strength of porous ceramics. Smaller pore sizes usually correspond to higher compressive strengths because the pore walls around the smaller pores are more likely to maintain structural integrity when subjected to external forces. The distribution and morphology of pores will also affect the compressive strength of porous ceramics. Uniformly distributed pore structures usually provide better mechanical properties on account of the fact that they can disperse stress more evenly. The above-mentioned influencing factors can be expressed in terms of three Equations (11)–(13) to express their relationship with compressive strength [40]:

$$\sigma = \sigma_0(1 - P)^n \tag{11}$$

$$\sigma = \sigma_0\left(\frac{d_0}{d}\right)^m \tag{12}$$

$$\sigma = \sigma_0 \cdot {}^{\left(-\frac{P}{P_0}\right)} \tag{13}$$

σ is the compressive strength of the porous ceramic, MPa; σ_0 is the compressive strength of the dense ceramic, MPa; P is the porosity, %; n is a constant, usually between 2 and 3; d is the pore size of the porous ceramic, m; d_0 is the reference pore size of the dense ceramic, m; m is a constant, usually between 1 and 2; P_0 is a constant, usually related to the microstructure of the material.

When the SiC content was increased from 0 wt.% to 2 wt.%, the compressive strength of the samples decreased. This reduction is attributed to the gas generation from SiC, which accelerates the growth of pores in the liquid phase during the sintering process. Conversely, the apparent porosity and water absorption of the samples with SiC content ranging from 0 to 2 wt.% increased significantly. This increase can be attributed to the excess SiC, which causes the pressure difference between the interior and exterior of the pores to exceed their surface tension. As a result, pores tend to bind together, collapse, and form interconnected structures. This phenomenon leads to an increase in apparent porosity and water absorption.

Figure 7 illustrates the properties of samples added with 0.5 wt.% and 1 wt.% SiC content under varying temperature conditions. The data indicate that the properties of the samples fluctuate with changes in sintering temperature. Specifically, as the sintering temperature rises from 1200 °C to 1220 °C, the compressive strength of the 0.5 wt.% and 1 wt.% SiC-added samples decreases from 13.3 MPa and 8.4 MPa to 6.8 MPa and 5.3 MPa, respectively. Concurrently, the bulk density declines from 1.31 g/cm^3 and 1.17 g/cm^3 to 1.07 g/cm^3 and 0.92 g/cm^3 (Figure 7a,c). Notably, both compressive strength and bulk density exhibit a consistent decreasing trend with increasing temperature. In contrast, water absorption and apparent porosity increase, with values rising from 14.5% and 31.1% to 24.1% and 43.1%, and from 14.1% and 31.2% to 31.9% and 39.7%, respectively. These observations can be attributed to several factors. At a calcination temperature of 1200 °C, the viscosity of the liquid phase decreases significantly. Additionally, the reaction rate between SiC and O_2 accelerates due to the temperature gradient within the material and the presence of sufficient SiC. Furthermore, the internal pressure within the pores exceeds their surface tension, leading to pore rupture and an increase in water uptake [41]. However, excessively

high sintering temperatures may lead to coalescence, collapse, and migration of pores from the interior to the surface of the material, as depicted in Figure 8a. This phenomenon can further enhance the water absorption and apparent porosity of the material.

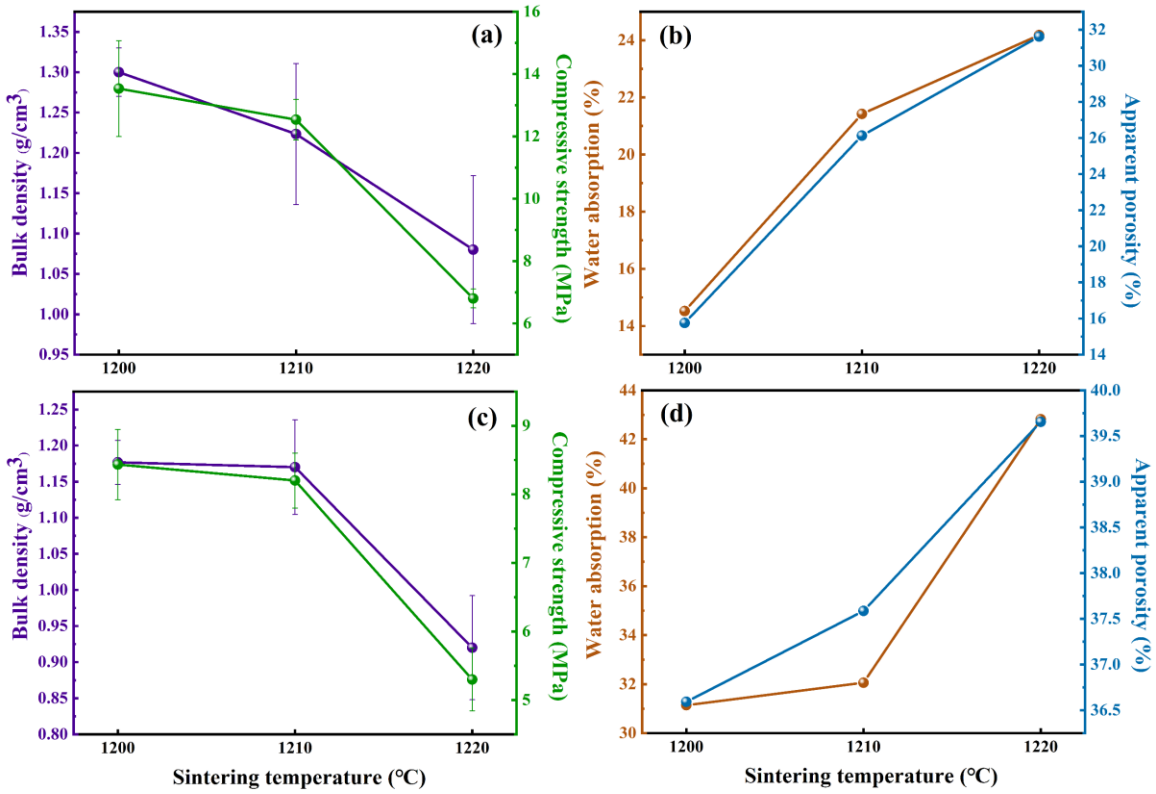

Figure 7. Compressive strength, bulk density, apparent porosity, and water absorption of foamed ceramics prepared at various sintering temperatures (1200 °C, 1210 °C, 1220 °C) with SiC content of (**a**,**b**) 0.5 wt.%, (**c**,**d**) 1 wt.%.

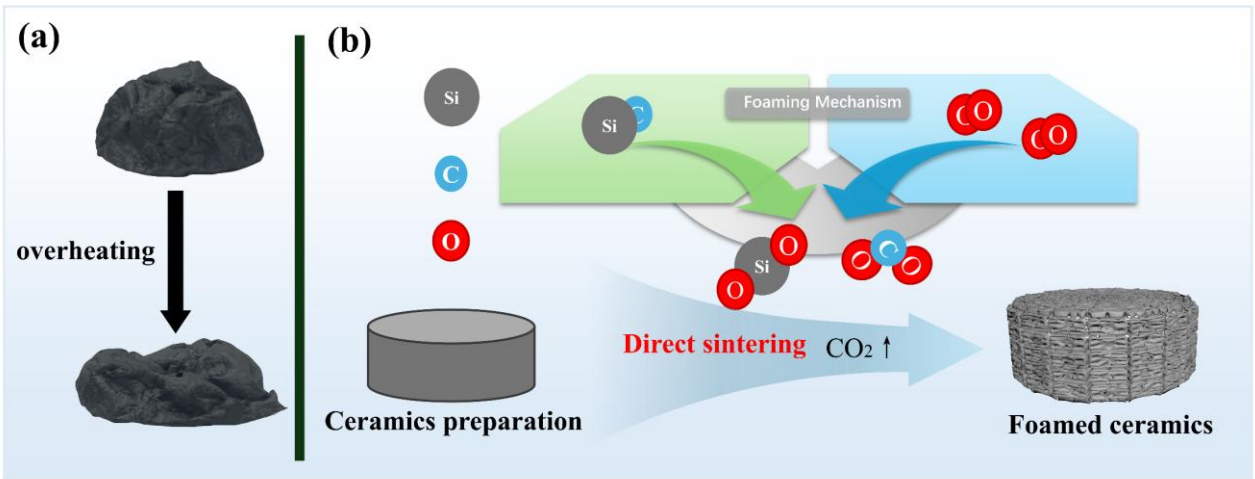

Figure 8. (**a**) Melting and collapsing caused when the sample is overheating; (**b**) diagram of foaming mechanism.

Figure 8b describes the foaming mechanism of the whole experiment. The foaming mechanism of fly ash and red mud-based materials is significantly influenced by the choice of foaming agent. Effective foaming agents, such as SiC, TiN, and carbonate compounds (e.g., $CaCO_3$), can lead to the production of foaming materials with excellent performance.

Based on previous experimental results, SiC was selected as the foaming agent for this study. In a high-temperature oxidizing atmosphere, SiC undergoes oxidation, resulting in the generation of CO_2. The corresponding reaction equation is as follows:

$$SiC(s) + 2O_2 = SiO_2 + CO_2\uparrow \quad (14)$$

The early oxidation products of SiC lead to the formation of a glassy SiO_2 film. As the temperature rises to between 800 and 1140 °C, the glassy SiO_2 film undergoes crystallization. The resulting phase transition induces a change in the volume of the SiO_2 protective film, causing it to become loose. Consequently, the adhesion between the SiO_2 film and the SiC substrate weakens, resulting in a sudden decrease in the oxidation protection provided by the film. Additionally, the oxidation reaction of silicon carbide generates gaseous byproducts, which can lead to foaming phenomena, further compromising the effectiveness of the SiO_2 film as an oxidation barrier [42].

4. Conclusions

The structure, crystalline phase, and properties of samples derived from fly ash and red mud as raw material were systematically characterized under varying temperatures and SiC content. The results indicated that the foamed ceramics produced with 1 wt.% SiC exhibited the most homogeneous pore distribution and optimal properties at a sintering temperature of 1210 °C. Specifically, the compressive strength, bulk density, apparent porosity, water absorption, linear expansion rate, and vertical expansion rate were 8.2 MPa, 1.173 g/cm^3, 37.58%, 32.06%, 18.93%, and 151.83%, respectively. The primary crystalline phases identified in the resulting foamed ceramics included sillimanite, anorthite, and hematite. Notably, there was no significant change in the composition of the crystalline phase across the experimental variables. However, the strength, macrostructure, microstructure, and properties were all significantly impacted by the SiC ratio and the sintering temperature, with further analyses revealing that the SiC proportion was more critical than temperature. In conclusion, these findings contribute to the effective utilization of fly ash and red mud in the preparation of cost-effective, high-performance foamed ceramics. This type of foamed ceramics not only consumes and utilizes solid waste but also has a broad application prospect in the fields of building thermal insulation and industrial kiln thermal insulation.

Author Contributions: Resources, X.S., Z.L. and X.F.; writing—original draft preparation, J.W. and X.Z.; writing—review and editing, X.S., Z.L. and X.F.; visualization, M.F., Y.Y., G.G. and Z.G.; supervision, X.S., Z.L. and X.F.; funding acquisition, X.S., Z.L. and X.F. All authors have read and agreed to the published version of the manuscript.

Funding: This work was supported by Natural Science Research Projects of Anhui Universities (KJ2021A0428), Bonanza Precision Mining and Environmental Protection (Guizhou Provincial Academician Expert Workstation, KXJZ[2024]003), Anhui International Joint Research Center for Nano Carbon-based Materials and Environmental Health (NCMEH2024Y01), Scientific Research Foundation for High-level Talents of Anhui University of Science and Technology (2021yjrc49), Anhui Provincial Natural Science Foundation (2208085QE171), the University Synergy Innovation Program of Anhui Province (GXXT-2023-019, GXXT-2022-083), National Natural Science Foundation of China (NSFC) (52227901), Graduate Innovation Fund of Anhui University of Science and Technology (2024cx2090), Innovation and Entrepreneurship Training Program for Undergraduates (202310361017, 202410361018).

Data Availability Statement: The original contributions presented in this study are included in the article. Further inquiries can be directed to the corresponding authors.

Acknowledgments: This present work was supported by Analytical and Testing Center (Anhui University of Science and Technology) and Key Laboratory of Industrial Dust Prevention and Control & Occupational Health and Safety (Ministry of Education, Anhui University of Science and Technology).

Conflicts of Interest: The authors declare no conflicts of interest.

References

1. Niu, A.; Lin, C. Trends in research on characterization, treatment and valorization of hazardous red mud: A systematic review. *J. Environ. Manag.* **2024**, *351*, 119660. [CrossRef]
2. Chai, Z.; Chen, X.; Fang, M.; Min, X.; Huang, Z.; Wang, Q.; Liu, C.; Liu, Y.; Huang, F. Fabrication and properties of high-thermal-storage RTO ceramics using bauxite tailings and red mud. *Ceram. Int.* **2023**, *49*, 31342–31350. [CrossRef]
3. Xu, W.; She, K.; Cao, Z.; Li, F.; Zhang, Y.; Zhang, T.; Wu, N.; Ouyang, S. Crystallization and thermal stability effects on tailings glass-ceramics by various heat-treating processes. *Mater. Chem. Phys.* **2021**, *263*, 124334. [CrossRef]
4. Bhatnagar, A.; Vila,r V.J.P.; Botelho, C.M.S. A review of the use of red mud as adsorbent for the removal of toxic pollutants from water and wastewater. *Environ. Technol.* **2011**, *32*, 231–249. [CrossRef] [PubMed]
5. Das, D.; Rout, P.K. A review of coal fly ash utilization to save the environment. *Water Air Soil Pollut.* **2023**, *234*, 128. [CrossRef]
6. Carlson, C.L.; Adriano, D.C. Environmental impacts of coal combustion residues. *J. Environ. Qual.* **1993**, *22*, 227–247. [CrossRef]
7. Chen, H.J.; Shih, H.; Wu, C.; Lin, S. Effects of the loss on ignition of fly ash on the properties of high-volume fly ash concrete. *Sustainability* **2019**, *11*, 2704. [CrossRef]
8. Xenidis, A.; Harokopou, A.D.; Mylona, E. Modifying alumina red mud to support a revegetation cover. *JOM* **2005**, *57*, 42–46. [CrossRef]
9. Wang, J.; Lu, D.; Xuan, W. Boron nitride micro ribbons strengthened and toughened alumina composite ceramics with excellent mechanical, dielectric, and thermal conductivity properties. *J. Adv. Ceram.* **2024**, *13*, 496–506. [CrossRef]
10. Brunori, C.; Cremisini, C.; Massanisso, P. Reuse of treated red mud bauxite waste: Studies on environmental compatibility. *J. Hazard. Mater.* **2005**, *117*, 55–63. [CrossRef]
11. Pan, Z.; Cheng, L.; Lu, Y.; Yang, N. Hydration products of alkali-activated slag–red mud cementitious material. *Cem. Concr. Res.* **2002**, *32*, 357–362. [CrossRef]
12. Li, Y.; Liu, C.; Luan, Z.; Peng, X.; Zhu, C.; Chen, Z.; Zhang, Z.; Fan, J.; Jia, Z. Phosphate removal from aqueous solutions using raw and activated red mud and fly ash. *J. Hazard. Mater.* **2006**, *137*, 374–383. [CrossRef] [PubMed]
13. Zhang, X.; Chen, X.; Min, W.; Liang, G.; Zhang, W.; Yao, S.; Zhong, X. Preparation of multifunctional ceramic foams for sound absorption, waterproofing, and antibacterial applications. *RSC Adv.* **2024**, *14*, 1009–1017. [CrossRef] [PubMed]
14. Yoon, S.D.; Yun, Y.H. An advanced technique for recycling fly ash and waste glass. *J. Mater. Process. Technol.* **2005**, *168*, 56–61. [CrossRef]
15. Leroy, C.; Ferro, M.C.; Monteiro, R.C. Production of glass-ceramics from coal ashes. *J. Eur. Ceram. Soc.* **2001**, *21*, 195–202. [CrossRef]
16. Shen, X.; Wu, K.; Sun, H.; Sang, L.; Huang, Z.; Lmura, M.; Koide, Y.; Koizumi, S.; Liao, M. Temperature dependence of Young's modulus of single-crystal diamond determined by dynamic resonance. *Diam. Relat. Mater.* **2021**, *116*, 108403. [CrossRef]
17. Huo, W.; Zhang, X.; Chen, Y.; Wang, D.; Liu, J.; Yan, S.; Yang, J. Mechanical strength of highly porous ceramic foams with thin and lamellate cell wall from particle-stabilized foams. *Ceram. Int.* **2018**, *44*, 5780–5784. [CrossRef]
18. Chen, G.; Shen, C.; Zhou, L. Design and performance analysis of wireless sensor network location node system for underground mine. *Min. Sci. Technol.* **2009**, *19*, 813–818. [CrossRef]
19. Lv, Z.; Cao, Y.; Lan, C.; Fan, M.; Ke, Y.; Guo, W.; Yang, Y.; Wang, X.; Shen, X. Property dependence on particle size and sintering temperature of waste porcelain high-temperature resistant material. *Int. J. Appl. Ceram. Technol.* **2025**, *22*, e14890. [CrossRef]
20. Li, C.; Gao, R.; Ouyang, H. Hierarchical porous $(Ta_{0.2}Nb_{0.2}Ti_{0.2}Zr_{0.2}Hf_{0.2})C$ high-entropy ceramics prepared by a self-foaming method for thermal insulation. *J. Adv. Ceram.* **2024**, *13*, 956–966. [CrossRef]
21. Yu, G.; Gao, W.; Yao, Y.; Zhang, T.; Fu, Y.; Kong, X. Recycling of silicomanganese slag and fly ash for preparation of environment-friendly foamed ceramics. *Materials* **2023**, *16*, 6724. [CrossRef] [PubMed]
22. Shi, X.; Li, K.; Shen, Z. $BS_{0.5}$BNT-based relaxor ferroelectric ceramic/glass-ceramic composites for energy storage. *J. Adv. Ceram.* **2023**, *12*, 695–710. [CrossRef]
23. Fu, F.; Hu, N.; Yang, S.; Li, Q.; Ye, Y.; Tang, R.; Chen, G. Effect of green gel system upon the properties of phosphorus tailings foamed ceramics. *Ceram. Int.* **2024**, *50 Pt A*, 38748–38760. [CrossRef]
24. Shao, J.; Bai, C.; Li, X. Open cell mullite ceramic foams derived from porous geopolymer precursors with tailored porosity. *J. Adv. Ceram.* **2023**, *12*, 279–295. [CrossRef]

25. Zhang, L.; Hu, D.; Snetkov, I.L. A review on magneto-optical ceramics for Faraday isolators. *J. Adv. Ceram.* **2023**, *12*, 873–915. [CrossRef]
26. Xu, X.; Zhang, J.; Wu, J.; Chen, Z.; Wang, Y. Preparation of foamed ceramics from steel slag with high calcium and iron content. *Int. J. Appl. Ceram. Technol.* **2023**, *20*, 2993–3003. [CrossRef]
27. Li, X.; Sun, D.; Yang, Q.; Lv, C. Foaming performance of the closed–pore foamed ceramics using silicon nitride as a foaming agent and sodium tetraborate as a modifier of foaming. *J. Eur. Ceram. Soc.* **2021**, *41*, 6330–6337. [CrossRef]
28. Li, X.; Yang, Q.; Sun, D.; Lv, C. Foaming mechanism and performance of closed–pore foamed ceramics prepared using calcium carbonate as a foaming agent. *Ceram. Int.* **2021**, *47*, 29162–29173. [CrossRef]
29. Wu, Z.; Zhao, Y.; Li, H.; Zeng, X.; Lin, J.; Wu, J.; Zhou, Y.; Chen, G.; Lai, X. Multifunctional ceramifiable silicone foam for smart firefighting. *Chem. Eng. J.* **2024**, *496*, 154149. [CrossRef]
30. Zhou, L.; Liu, J.; Tu, T. Fast grain growth phenomenon in high-entropy ceramics: A case study in rare-earth hex aluminates. *J. Adv. Ceram.* **2023**, *12*, 111–121. [CrossRef]
31. Cengizler, H.; Koç, M.; Şan, O. Production of ceramic glass foam of low thermal conductivity by a simple method entirely from fly ash. *Ceram. Int.* **2021**, *47*, 28460–28470. [CrossRef]
32. Luo, Y.; Zheng, S.; Ma, S.; Liu, C.; Wang, X. Preparation of sintered foamed ceramics derived entirely from coal fly ash. *Constr. Build. Mater.* **2018**, *163*, 529–538. [CrossRef]
33. Xia, F.; Cui, S.; Pu, X. Performance study of foam ceramics prepared by direct foaming method using red mud and K-feldspar washed waste. *Ceram. Int.* **2022**, *48*, 5197–5203. [CrossRef]
34. Dry, C.; Meier, J.; Bukowski, J. Sintered coal ash/flux materials for building materials. *Mater. Struct.* **2004**, *37*, 114–121. [CrossRef]
35. Giergiczny, Z. Fly ash and slag. *Cem. Concr. Res.* **2019**, *124*, 105826. [CrossRef]
36. Huang, J.; Yuan, J.; Zhu, T.; Zhong, T.; Xu, Y.; Lou, S. Dynamic compressive strength of alumina ceramics. *Ceram. Int.* **2022**, *48*, 36371–36382. [CrossRef]
37. Huang, Y.; Hu, N.; Ye, Y.; Ou, Z.; Shi, X. Preparation and pore-forming mechanism of MgO–Al_2O_3–CaO-based porous ceramics using phosphorus tailings. *Ceram. Int.* **2022**, *48*, 29882–29891. [CrossRef]
38. Wang, R.; Liu, X.; Wei, H.; Xu, Y.; Zhou, R.; Huang, Z.; Zhan, H.; Ma, S.; Yang, C. Study on phase behavior and mechanical properties of high temperature resistant materials prepared from waste electric porcelain. *Ceram. Int.* **2023**, *49*, 11537–11543. [CrossRef]
39. Dong, X.; Han, F.; Hua, W.; Liu, T.; Zheng, J.; An, C.; Li, M. Preparation and properties of microcrystalline foam ceramics from silicon manganese smelting slag. *Ceram. Int.* **2024**, *50 Pt B*, 2073–2082. [CrossRef]
40. Shi, X.; Liao, Q.; Liu, L.; Deng, F.; Chen, F.; Wang, F.; Zhu, H.; Zhang, L.; Liu, C. Utilizing multi-solid waste to prepare and characterize foam glass ceramics. *Ceram. Int.* **2023**, *49 Pt A*, 35534–35543. [CrossRef]
41. Fu, F.; Hu, N.; Ye, Y.; Chen, G.; Jia, J. Production of lightweight foam ceramics by adjusting sintering time and heating rate. *Constr. Build. Mater.* **2023**, *394*, 132064. [CrossRef]
42. Cao, Y.; Lv, Z.; Zhang, K.; Lan, C.; Fan, M.; Lu, X.; Ke, Y.; Guo, W.; Yang, Y.; Wang, X.; et al. Waste electric porcelain-based refractory bricks with significantly enhanced mechanical properties: Preparation, characterization and mechanism. *Ceram. Int.* **2024**, *50 Pt A*, 49698–49711. [CrossRef]

Disclaimer/Publisher's Note: The statements, opinions and data contained in all publications are solely those of the individual author(s) and contributor(s) and not of MDPI and/or the editor(s). MDPI and/or the editor(s) disclaim responsibility for any injury to people or property resulting from any ideas, methods, instructions or products referred to in the content.